PHYSICAL REVIEW E **94**, 033112 (2016)

Coalescence of sessile microdroplets subject to a wettability gradient on a solid surface

Majid Ahmadlouydarab,[1] Chuanjin Lan,[1] Arup Kumar Das,[2] and Yanbao Ma[1]
[1]*School of Engineering, University of California, Merced, California 95343, USA*
[2]*Department of Mechanical and Industrial Engineering, IIT Roorkee, Roorkee 247667, India*

(Received 8 April 2016; revised manuscript received 24 June 2016; published 20 September 2016)

While there are intensive studies on the coalescence of sessile macroscale droplets, there is little study on the coalescence of sessile microdroplets. In this paper, the coalescence process of two sessile microdroplets is studied by using a many-body dissipative particle dynamics numerical method. A comprehensive parametric study is conducted to investigate the effects on the coalescence process from the wettability gradient, hydrophilicity of the solid surface, and symmetric or asymmetric configurations. A water bridge is formed after two microdroplets contact. The temporal evolution of the coalescence process is characterized by the water bridge's radii parallel to the solid surface (W_m) and perpendicular to the solid surface (H_m). It is found that the changes of both H_m and W_m with time follow a power law; i.e., $H_m = \beta_1\tau^\beta$ and $W_m = \alpha_1\tau^\alpha$. The growth of H_m and W_m depends on the hydrophilicity of the substrate. W_m grows faster than H_m on a hydrophilic surface, and H_m grows faster than W_m on a hydrophobic surface. This is due to the strong competition between capillary forces induced by the water-bridge curvature and the solid substrate hydrophobicity. Also, flow structure analysis shows that regardless of the coalescence type once the liquid bridge is formed the liquid flow direction inside the capillary bridge is to expand the bridge radius. Finally, we do not observe oscillation of the merged droplet during the coalescence process, possibly due to the significant effects of the viscous forces.

DOI: 10.1103/PhysRevE.94.033112

I. INTRODUCTION

The coalescence of droplets is a fundamental flow phenomenon with broad applications, including digital microfluidic mixing, painting, condenser design, surface cleaning, ink-jet printing, powder metallurgy, and so on [1–9]. The coalescence can occur between two or multiple droplets, or between a droplet and a liquid pool. It can occur either on a solid surface or inside a liquid pool. When it occurs inside a liquid pool, the process is called free coalescence.

Significant research has been done to address the different aspects of the physics involved in free coalescence processes [10–13]. A free coalescence process is governed by capillary, viscous, and inertial forces, which can be characterized by two determinant parameters: The Reynolds number (a ratio of inertial force to viscous force) and the Weber number (a ratio of inertial force to capillary force). The Weber number is defined as $\mathrm{We} = 2R\rho U_r^2/\sigma$. Where R is the droplet radius, U_r the relative velocity, ρ the droplet density, and σ the surface tension. The capillary forces accelerate the coalescence process, while the viscous forces decelerate the coalescence process. There exists a criterion in terms of a minimum Weber number for a successful free coalescence process [1,9]. In the early stage of coalescence, a capillary bridge is formed after two droplets contact each other. The growth rate of the bridge has received much attention. A general form for the growth rate of the bridge's radius is given through $R(t) = At^B$. Here A is an empirical coefficient and B mainly depends on whether the coalesces process is viscous or inertial [14–17].

Compared with a free coalescence process, the existence of the solid surface in a coalescence process of sessile droplets introduces two new features, including friction force and the dynamics of a triple contact line [18]. These new features may cause asymmetric growth of the formed capillary bridge between two sessile droplets depending on the surface conditions [19]. Up to now, several techniques have been developed to move the sessile droplets towards each other so that they can coalesce. Among these, there is the gradient surface technique in which a wetting gradient on the solid substrate is created and a droplet is driven by capillary forces. Different methods for the generation of a wettability-gradient surface, including vapor-phase diffusion, thermal, electrochemical, photolithographic, gradual immersion, photoinitiator-mediated photopolymerization, corona treatment, contact printing, microfluidic device, and microstructure, have been developed [20–32].

The analysis of the coalescence process between two sessile droplets on a solid surface can be divided into two main stages: early-stage coalescence, in which there is rapid initial growth of the liquid bridge connecting two droplets, and late-stage coalescence, in which the shape of the combined drop goes through a slow rearrangement from an elliptical or peanut shape to a hemispherical shape to minimize its free surface energy [33]. Late-stage coalescence has drawn lots of attention in the past decade [3,34,35]. Recently, researchers have begun to explore the early stage of the coalescence, which is vital in some applications where droplets mix together, spread on solid substrates, or condense [36,37]. For example, the rapid mixing of different reactants and reagents are a primary objective in microfluidic devices [9,37,38]. Similar to the free coalescence process, it has been found that the radius of the formed liquid bridge (meniscus) between two sessile droplets follows the power law, i.e., $R = \alpha\tau^\beta$, where R is radius, τ is time, and α and β are coefficients [15]. The power law for the growth of a liquid bridge in the early stage of coalescence of two sessile droplets has been validated in both experiments and numerical simulations [13,14,39].

So far, most of the previous studies of coalescence process have focused on the externally measurable properties such as formed bridge (meniscus) radius, combined droplet radius, and contact angle. Very few of them have studied the flow structures during the coalescence process. For example, Lai *et al.*, using micro-PIV (Particle Image Velocimetry) technique, tracked the internal flow inside the combined droplet at a late stage of coalescence [9]. It was found that the released surface energy creates a pair recirculation flow inside the merged droplet and most released surface energy is converted into flow oscillation which eventually dies down through viscous dissipation [9]. However, there have been very few studies of the flow structures in the early stage of coalescence process, mainly due to the technical difficulties in capturing the fast coalescence process. In addition, most of the study of droplet coalescence focuses on macroscale droplets and there are very few studies of microdroplet coalescence. It should be noted that nowadays the droplet-based microfluidic systems have a wide range of benefits, such as rapid mixing of chemical fluids, medical agents, and other kinds of fluids, as well as less risk of reagent loss [40]. However, there is a lack of knowledge, in particular, in understanding the flow structures inside the merging microdroplets, as well as coalescence process on the solid substrates.

This paper aims to fill the knowledge gap on the coalescence process of sessile microdroplets. An in-house-developed numerical tool based on a many-body dissipative particle dynamics (MDPD) method is utilized in this study. We mainly focus on the flow physics of the coalescence process between a pair of sessile microdroplets driven by capillary forces induced by a wetting gradient on the solid substrate. Especially, the effects on the coalescence process from the surface wettability gradient, hydrophilicity of the solid surface, and symmetric or asymmetric initial configurations are studied through parametric numerical simulations. We hope this study not only advances our knowledge on the coalescence of sessile microdroplets, but also provides guidance for the manipulation of microdroplets in digital microfluidic design and other applications.

II. PROBLEM SETUP AND METHODOLOGY

A. Computational domain setup

The physical domain consists of a three-dimensional (3D) rectilinear cube of size $2L \times Y \times Z$ in the x, y, and z directions, respectively. The origin of the coordinates is located in the center of the computational domain. Figure 1 shows two sessile microdroplets of diameters R_1 and R_2 located at $x = L_1$ and $x = -L_2$, respectively. The contact angle decreases linearly from θ_0 at $x = -L$ to θ_f at $x = 0$; then it increases linearly to θ_0 at $x = L$. The wettability gradient is used to drive both microdroplets towards the center for the study of coalescence. There is no wettability gradient in the y direction. The numerical method is described in next section.

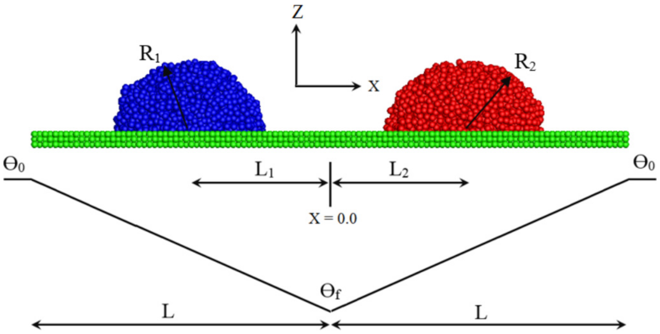

FIG. 1. Schematic of the initial configuration for 3D computations.

B. Numerical method

1. Dissipative particle dynamics and many-body dissipative particle dynamics

A dissipative particle dynamics (DPD) method and its modified version, a many-body dissipative particle dynamics (MDPD), method are mesh-free particle-based methods that have successfully been used to simulate mesoscale fluid mechanical problems [41–44]. In this method, fluid is modeled as a group of beads. The motion of each bead is governed by Newton's second law,

$$\frac{d\overrightarrow{r_i}}{dt} = \overrightarrow{v_i}, \tag{1}$$

$$m_i \frac{d\overrightarrow{v_i}}{dt} = \overrightarrow{f_i} = \sum_{i \neq j} \left(\overrightarrow{F_{ij}^C} + \overrightarrow{F_{ij}^D} + \overrightarrow{F_{ij}^R}\right), \tag{2}$$

where $\overrightarrow{r_i}$, $\overrightarrow{v_i}$, and $\overrightarrow{f_i}$ denote the ith bead's position, velocity, and the total force imposed on that bead, respectively. The three components of $\overrightarrow{f_i}$, including conservative force $\overrightarrow{F_{ij}^C}$, dissipative force $\overrightarrow{F_{ij}^D}$, and random force $\overrightarrow{F_{ij}^R}$, are given by Eqs. (3), (4), and (5) [41,45]:

$$\overrightarrow{F_{ij}^C} = \alpha \omega_C(r_{ij}) \overrightarrow{e_{ij}}, \tag{3}$$

$$\overrightarrow{F_{ij}^D} = \gamma \omega_D(r_{ij}) (\overrightarrow{e_{ij}} \cdot \overrightarrow{v_{ij}}) \overrightarrow{e_{ij}}, \tag{4}$$

$$\overrightarrow{F_{ij}^R} = \varphi \omega_R(r_{ij}) \theta_{ij} (\delta_t)^{-1/2} \overrightarrow{e_{ij}}. \tag{5}$$

Here $r_{ij} = |\overrightarrow{r_{ij}}|$, $\overrightarrow{r_{ij}} = \overrightarrow{r_i} - \overrightarrow{r_i}$, $\overrightarrow{e_{ij}} = \overrightarrow{r_{ij}}/|r_{ij}|$, and $\overrightarrow{v_{ij}} = \overrightarrow{v_i} - \overrightarrow{v_j}$. ω_C, ω_D, and ω_R are weight functions for conservative, dissipative, and random forces, respectively. θ_{ij} is the Gaussian white noise with zero mean and unit variance. α, γ, and φ are the amplitudes of conservative, dissipative, and random forces, respectively. If the dissipation parameter γ and the white-noise amplitude δ_t satisfy the fluctuation-dissipation theorem, then the dissipative and random forces act as a thermostat. This requires $\omega_D(r) = [\omega_D(r)]^2$ and $\varphi^2 = 2\gamma k_B T$, where k_B is the Boltzmann constant and T is the temperature of the system. Commonly, the weight functions are chosen as below:

$$\omega_C(r_{ij}) = \begin{cases} 1 - \frac{r_{ij}}{r_c}, & r < r_c, \\ 0, & r \geqslant r_c, \end{cases} \tag{6}$$

$$\omega_D(r) = [\omega_R(r)]^2 = \begin{cases} \left(1 - \frac{r_{ij}}{r_c}\right)^2, & r < r_c, \\ 0, & r \geqslant r_c. \end{cases} \tag{7}$$

The main limitation of the DPD method is its inability to model liquid-gas two-phase flow. To remove this limitation, Warren presented a MDPD method, a modified version of

DPD. In MDPD, an attractive force is introduced in addition to a repulsive force in the calculation of conservative forces,

$$\overrightarrow{F_{ij}^{C}} = A_{ij}\omega_C(r_{ij}) + B_{ij}(\overline{\rho_i} + \overline{\rho_j})\omega_d(r_{ij}), \tag{8}$$

where A_{ij} and B_{ij} are the amplitudes of attractive and repulsive forces, respectively,

$$\omega_d(r_{ij}) = \begin{cases} 1 - r_{ij}/r_d, & r < r_d, \\ 0, & r \geqslant r_d. \end{cases} \tag{9}$$

In Eq. (8), the repulsive part depends on a weighted average of bead density and the attractive part is density independent. To calculate the density of each bead Eq. (10) is used:

$$\bar{\rho}_i = \sum_{i \neq j} 15 \big/ \left(12\pi r_{ij}^3\right)(1 - r_{ij}/r_d)^2. \tag{10}$$

In this study, we adopt the MDPD method to simulate the coalescence process of two sessile microdroplets. Because the gravity force is negligible compared to the capillary force, gravity is not considered in this study. Moreover, temporal integration is performed using a modified velocity-Verlet algorithm in the MDPD simulations [41].

2. *Boundary conditions and adopted parameters*

The driving force for droplet motion is the capillary force induced by the adopted wetting gradient on the solid substrate. The contact angle (θ) on the solid surface can change from hydrophilic ($\theta < 90^\circ$) to hydrophobic ($\theta > 90^\circ$) by changing the surface wettability. In the implementation of the MDPD method, the wettability property is modeled by the attraction parameter A_{lw} between a liquid bead from the droplet and a solid bead from the substrate using Eq. (11). In this study, Eq. (11) is used to generate a symmetric wettability gradient in the x direction ranging from $x = -L$ to $x = L$:

$$A_{lw} = \begin{cases} -1.211 - \sqrt{552.125 - 3.3\theta_0}, & x < -L, \\ -1.211 - \sqrt{552.125 - 3.3\theta_0 + 3.3\frac{\theta_0 - \theta_f}{L}(x + L)}, & -L \leqslant x \leqslant 0, \\ -1.211 - \sqrt{552.125 - 3.3\theta_f + 3.3\frac{\theta_f - \theta_0}{L}x}, & 0 \leqslant x \leqslant L, \\ -1.211 - \sqrt{552.125 - 3.3\theta_0}, & x > L. \end{cases} \tag{11}$$

With this setup, the static contact angle decreases linearly from θ_0 at $x = -L$ to θ_f at $x = 0$; then it increases linearly back to θ_0 at $x = L$ [43]. In this study, the coalescence process between a moving droplet and a stationary one is considered as well. To this aim, the static contact angle on the solid substrate will keep a constant θ_f for the x locations in the range of $-L \leqslant x \leqslant 0.0$, or, equivalently, A_{lw} will remain a constant.

In general, the dynamic contact angle (θ_d) is considered as a function of the capillary number $\text{Ca} = \mu u/\sigma$, indicating the ratio viscous and capillary forces. In an analytical continuum treatment of dynamic wetting, a relationship between θ_d and Ca cannot be obtained directly by solving the momentum equations with no-slip boundary conditions. Indeed, to describe contact line (CL) motion, supplementary models for the microscopic region where the meniscus meets the solid boundary must be employed. As an advantage, such supplementary models are not required in DPD and MDPD calculations because the DPD and MDPD methodology can automatically capture the change of dynamic contact angles. It should be emphasized that any phenomenon of liquid flow is ultimately determined by the fundamental particle interactions and kinetics, which is the base for the DPD and MDPD methodology [46,47]. On the other hand, the literature shows that the generic behavior of CL dynamics can actually be understood in terms of an effective continuum model, even for small systems with a cutoff length scale comparable to the molecular size [48]. In MDPD and DPD calculations in extracting θ_d, a boundary layer of thickness $\sim r_c$ (cutoff radius) can been excluded, as within the small fluid wedge close to the CL [43,46,47]. Thus, the celebrated equation given by Cox [49] can be applied to relate the static contact angle (θ) to the dynamic or apparent contact angle (θ_d) as

$$\theta_d^3 - \theta^3 \cong 9\text{Ca}\ln(R_0/r_c), \tag{12}$$

where θ_d and θ are dynamic and static contact angles, respectively, Ca is the capillary number, R_0 is the initial microdroplet radius, and r_c is the cutoff radius in MDPD calculations. This equation has been validated in MDPD calculations [43,46,47]. In fact, compared with other mesh-based numerical methods that need dynamic contact angles as prerequisite boundary conditions, the capability of the particle-based MDPD method to automatically capture the hysteresis of the contact angles is a big advantage to simulate sessile droplets driven by a wettability gradient on a substrate. In the current study, the predicted maximum difference between dynamic and static contact angles is $\sim 1.5^\circ$.

In our MDPD calculations, the solid substrate is constructed from three layers of frozen solid beads as shown in Fig. 1. To avoid the penetration of liquid beads into the substrate, as well as to satisfy the no-slip boundary condition, a bounce-forward reflection boundary condition is used on the interface between the droplet and the substrate. In both x and y directions, which are parallel to the substrate surface, the periodic boundary condition is applied [43,44].

All parameters for MDPD calculations in the current study are listed in Table I in DPD units, and these parameters are the same as those used in Ref. [46]. In Table I, B_{ll} represents the repulsion between liquid (l) beads, while B_{lw} represents the repulsion between the substrate wall (w) and liquid (l) beads [45,50,51]. Like other DPD and MDPD studies [51], reduced nondimensional DPD units are used in this study such that length is measured in units of r_c (cutoff radius), energy in k_BT

TABLE I. The computational parameters used in MDPD simulations.

Parameters	Symbol	Value (DPD units)
Fluid bead density	ρ	6.00
Viscosity	μ	7.41
Surface tension	σ	7.51
System temperature	$k_B T$	1.00
Cutoff radius of attractive force	r_c	1.00
Cutoff radius of repulsive force	r_d	0.75
Amplitude of random force	φ	6.00
Attraction parameter	A_{ll}	– 40.00
Repulsion parameter	$B_{ll} = B_{lw}$	25.00
Time step	Δt	0.01

(T being the temperature and k_B the Boltzmann constant), and mass in liquid bead mass (m) [43]. To link the results from the DPD domain to the physical domain, one DPD length unit equals 10 μm in this study. Thus, a droplet with a diameter of 10 in DPD units has a diameter of 100 μm in the physical domain. The corresponding mass unit is $m = 1.67\times10^{-13}$ kg at a particle number density of $\rho = 6.0$, which gives a liquid density of 1.0×10^3 kg/m^3. The time unit is chosen as $t = 4.15$ μs so that the surface tension $\sigma = 7.50$ in the MDPD system corresponds to a liquid-vapor surface tension of 0.073 N/m.

It worth mentioning that in the current study a series of numerical simulations has been carried out with different numbers of particles to ensure the results are independent of particle numbers.

As discussed in the Introduction, it is common to use the formed capillary bridge's normalized dimensions H_m and W_m to quantify the coalescence process between a pair of sessile droplets. Figure 2 shows a schematic of the formed liquid bridge between two sessile droplets and the defined parameters H_m and W_m. H_m is the bridge height and W_m is one half of the bridge width. Both H_m and W_m are normalized by $2R_0$, where R_0 is the initial radius of one of the two droplets. The radii of two droplets are also normalized by R_0 to get R_{r1} and R_{r2}, respectively. Here we consider that the growth of H_m and W_m with time follows a power law in the form of $H_m = \beta_1\tau^\beta$ and $W_m = \alpha_1\tau^\alpha$, respectively. Both α and β will be extracted out from the simulation results. In addition, a nondimensional time $\tau = t\sigma/(\mu R_0)$ is defined for the convenience of discussion.

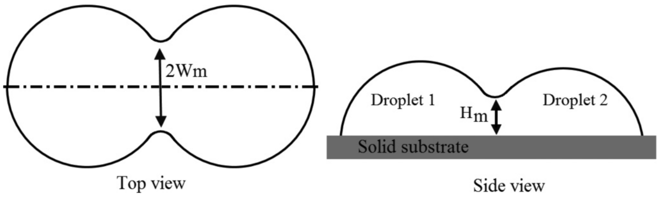

Top view Side view

FIG. 2. Schematic of top and side views of two coalesced sessile drops. W_m and H_m are shown in top and side views, respectively.

III. NUMERICAL RESULTS

A. Coalescence of two identical sessile droplets

1. Flow structure

In this section, we mainly focus on the growth of capillary bridge and flow analysis in coalescence processes of two identical sessile droplets. To study the effects on the coalescence process from different parameters including droplet sizes, surface wettability, hydrophilicity of the solid surface, and symmetric or asymmetric configurations, a baseline case is selected. Following are the parameters in the baseline case: $L_1 = L_2 = 12.5$, $L = 25.0$, $\theta_0 = 90^\circ$, $\theta_f = 82^\circ$, and $R_1 = R_2 = 5.0$ (see Fig. 1). In addition, the domain width and height are $Y = 40$ and $Z = 15$, respectively.

Before describing the general features of the two identical sessile droplets' coalescence, we briefly summarize the main results of flow analysis in single sessile droplets reported in our previous work [43]. These results can help to understand the flow mechanism in the coalescence process of two sessile droplets. In the previous study, it was found that the rolling, sliding, and combination of both are three motion modes for a sessile droplet, where wetting gradient and surface hydrophilicity are the determinant factors for different motion modes. For example, on a hydrophobic surface, rolling is the dominant mechanism while sliding becomes more important on the more hydrophilic surfaces. Moreover, it was found that there are strong flow circulations inside the sessile droplet regardless of solid surface hydrophilicity [43].

Here we consider the coalescence process of two identical sessile droplets on a the solid surface moving from opposite directions. The results of current study show that the initial complex flow structures inside each of the droplets change dramatically as coalescence process proceeds. Figure 3 shows a few 3D snapshots of the interfacial development and evolution of the coalescence process. Driven by opposite capillary forces, both droplets move toward the center of the computational domain [Fig. 3(a)]. Before the two droplets reach to the center of the computational domain ($x = 0$), their front faces touch each other and lead to the formation of a capillary bridge with a peanut shape of the merged droplet [Fig. 3(b)]. Then the bridge starts to grow in both parallel and perpendicular directions to the solid surface [Fig. 3(c)]. The peanut shape of the merged droplet in the early stage gradually changes to an elongated ellipsoid shape in a later stage of the coalescence process due to the growth of the capillary bridge [Fig. 3(d)]. Because the contact angles are close to 90°, there is nearly one-half of the peanut or elongated ellipsoid shape, as shown in Figs. 3(b) to 3(e). Finally, the merged droplet evolves to nearly a hemisphere shape at the end of the late-stage coalescence process [Fig. 3(f)].

To get better understanding of flow physics in the coalescence process, we conduct a flow analysis by tracking the trajectories of flow particles and taking the average in temporal domain to remove the effects on flow from Brownian motion. Figure 4 shows the 3D streamlines inside the coalescing droplets at three different coalescence stages: (a) very early stage, (b) early stage, and (c) late stage. It shows that the flow tends to expand the liquid bridge in both y and z directions. For the convenience of discussion, a contact zone is defined as a zone between two x planes, where the flow inside the liquid

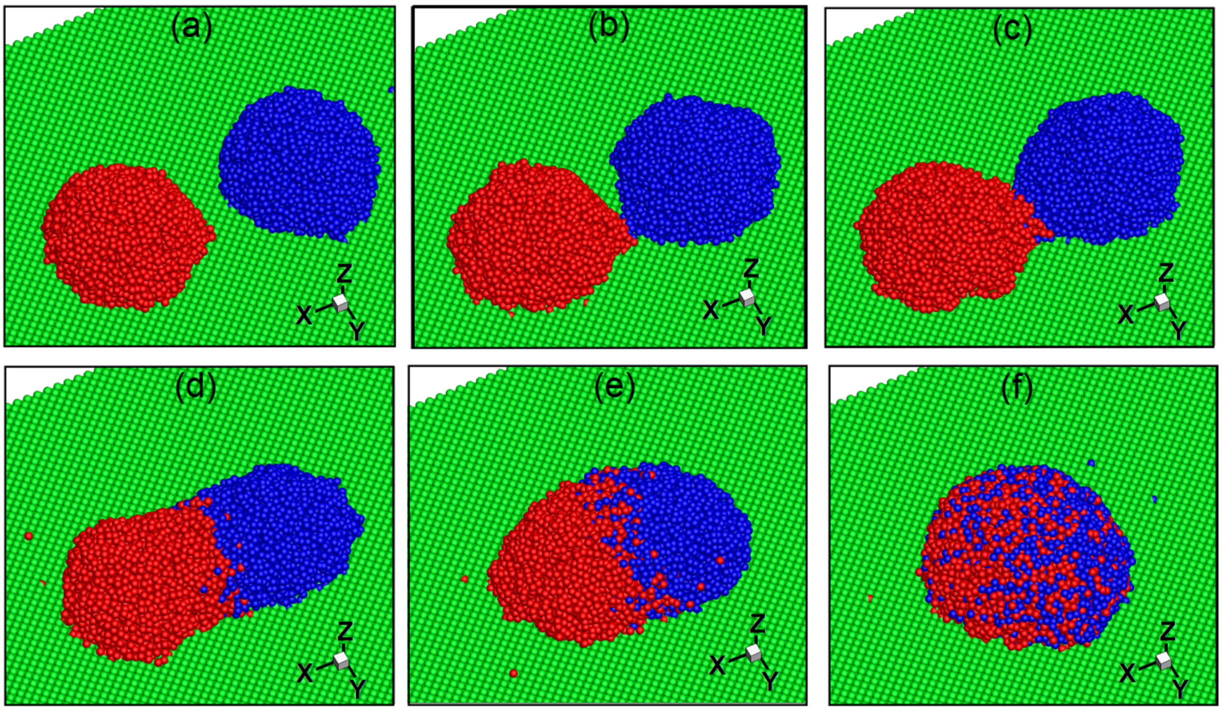

FIG. 3. Snapshots of the interfacial development and evolution of the coalescence process between a pair of identical sessile microdroplets. Note that time sequence is from (a) to (f).

bridge begins to divert to the direction perpendicular to the solid surface. In the early stage [Fig. 4(a)], the contact zone is almost the neck zone in the peanut-shaped merged droplet. As the coalescence evolves, the length of the contact zone increases in the x direction. Meanwhile, the formed water bridge expands in both y and z directions [see Fig. 4(b)]. Eventually, the length of the contact zone begins to decrease due to the expansion of the water bridge in both y and z directions and retraction of the merging droplet in the x direction due to the mass conservation. The length of the contact zone in the late stage shown in Fig. 4(c) is shorter than that in the early stage shown in Fig. 4(b).

In addition, due to the existence of nonaxisymmetric wetting gradient in the x direction, the final shape of the merged sessile droplet is not a perfect hemisphere. Flow analysis also indicates that the bridge does not grow symmetrically in different directions on the x plane due to the friction from the solid surface. This is in qualitative agreement with the results in Ref. [19]. More details on the quantitative study of the growth of the water bridge will be given in Sec. III A 2.

Figure 5 shows flow velocity vectors on the x, y, and z planes inside the merged droplet in an intermediate coalescence process with an elongated ellipsoid shape. The x plane is located at the center of the ellipsoid shape. In the x plane, there is flow in all different directions near the free surface, which leads to the expansion of the liquid bridge. The y plane is also located at the center of the ellipsoid droplet. There is flow from both ends of the ellipsoid droplet toward the center, which leads to shrinkage of the droplet in x direction and expansion in the z direction. The z plane is located a short distance from the solid surface. There is flow from both ends of the ellipsoid

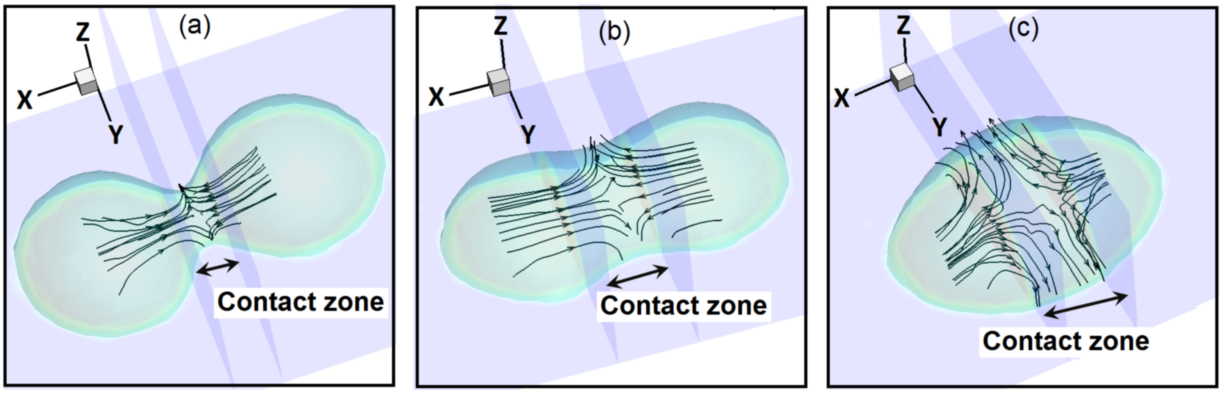

FIG. 4. Trimmed 3D flow streamlines inside the merged droplet at different arbitrary times during the symmetric coalescence process. Streamlines are released from arbitrarily selected x planes.

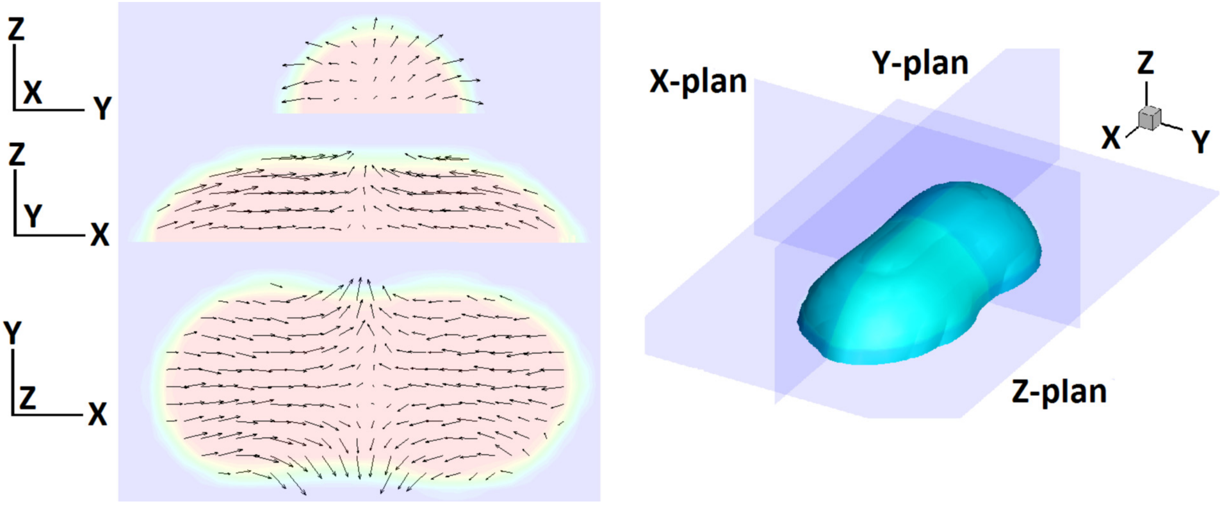

FIG. 5. Flow velocity vectors on the three different x, y, and z planes inside the merged droplet with an elongated ellipsoid shape (beginning of the late-stage coalescence).

toward the center. As a result, the droplet gradually changes from the ellipsoid shape to a hemisphere shape.

To quantify the initial coalescence process, dimensionless radiuses W_m and H_m (see Fig. 2) are calculated and compared with available data from literature. A modified Ohnesorge number $\mathrm{Oh} = \sigma\rho R_0/\mu^2$ is calculated according to Refs. [11,52] with parameters specified in Table I. This gives $\mathrm{Oh} = 4.11$, which indicates that the inertial coalescence driven by the capillary force is dominant over the viscous force. According to the results by Hernandez-Sanchez *et al.* [16], both W_m and H_m grow with time following a power law, i.e., $H_m = \beta_1\tau^\beta$ and $W_m = \alpha_1\tau^\alpha$. For the coalescence of macroscale droplets on a solid surface with a contact angle close to 90°, the values of β and α are reported around 0.5 in the literature [17,19]. Based on present numerical results, β and α are calculated as 0.54 and 0.55, respectively, which are close to the reported values in the literature.

2. *Substrate philicity effect*

It has been reported in the literature that the growth rate of the connecting bridge in the early stage of the coalescence of the macroscale droplets can be affected by the philicity of the solid substrate [17]. To study the effects on the coalescence of sessile microdroplets from the philicity of the substrate, we simulated three cases with the same wettability gradient but different sets of θ_0 and θ_f: (100°,92°), (90°,82°), and (70°,62°).

Our simulation results show that the flow structures for three cases are very similar to those reported in Sec. III A. However, there is quantitative difference in the growth of connecting bridge with time as shown in Fig. 6. If coalescence happens on a philic surface, e.g., $\theta_0 = 70°$ and $\theta_f = 62°$, the width of the capillary bridge (W_m) grows faster than its height (H_m) due to the stronger attractive forces between liquid and philic solid substrate. For $\theta_0 = 90°$ and $\theta_f = 82°$, both the width and the height of the capillary bridge grow at almost the same rate. However, further increase in the surface phobicity makes the bridge height grow faster than its width (see results for $\theta_0 = 100°$ and $\theta_f = 92°$) due to the stronger repulsive forces between the liquid and phobic solid surface.

Generally speaking, in the early stage of the sessile microdroplets coalescence process there is a strong competition between capillary forces induced from surface phobicity and water bridge curvature which is a determinant factor for the growth rates of W_m and H_m. On the other hand, our results do not predict oscillation of the merged droplet possibly due to the significant effects of the viscous forces.

B. Coalescence between sessile droplets of different sizes

For further understanding of the physics of the sessile microdroplets coalescence, we study the asymmetric coalescence process in this section. To this aim, the coalescence of two droplets with different sizes are considered. Then the results are compared with the those of the baseline model described in Sec. III A. While the radius of the first droplet R_1 is the same as that in the baseline model, the radius of the second droplet is given as 0.5, 1.0, and 1.5 for three different cases.

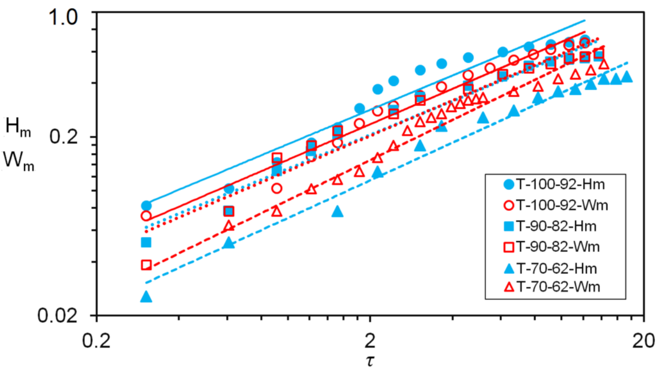

FIG. 6. Variation of W_m and H_m with time in the early stage of coalescence for different sets of (θ_0,θ_f). T-100-92-Hm and T-100-92-Wm are for (100°,92°), T-90-82-Hm and T-90-82-Wm are for (90°,82°), and T-70-62-Hm and T-70-62-Wm are for (70°,62°). Note that both the x and the y axes are in $\log_{10}$ scale.

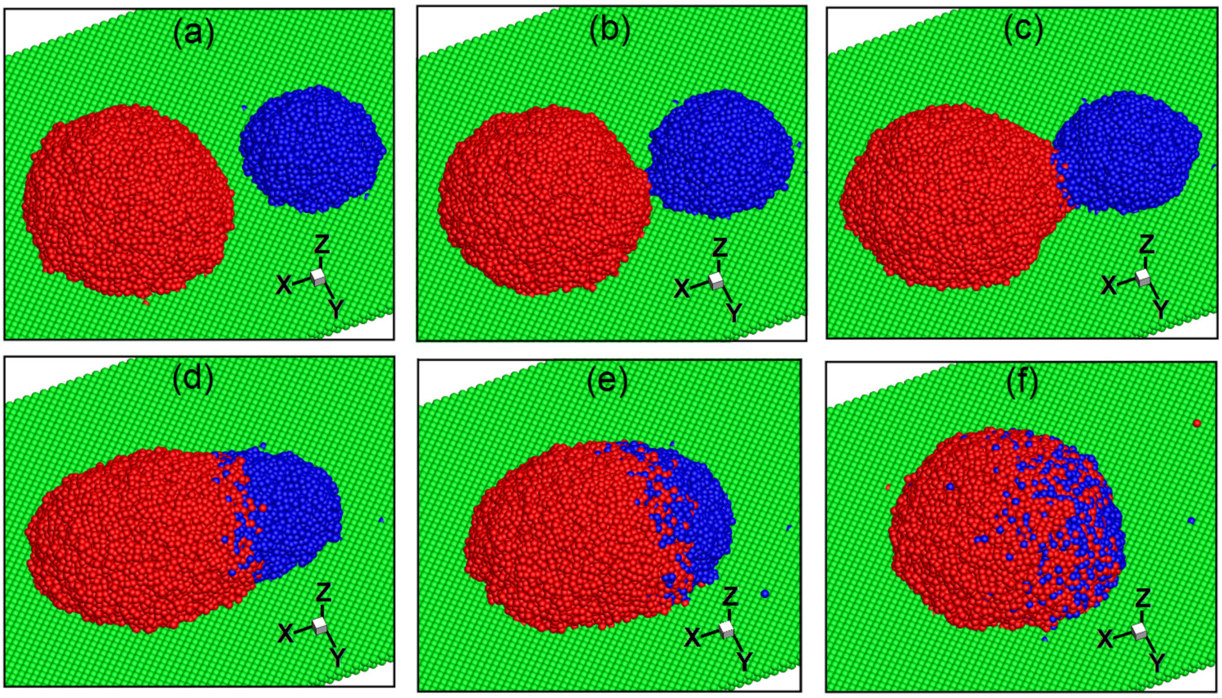

FIG. 7. Snapshots of the interfacial development and evolution of the coalescence process between a pair of sessile microdroplets of different sizes. Note that time sequence is from (a) to (f).

In the baseline case, the two identical droplets travel the same distance and the symmetric coalescence takes place near the center of the computational domain. For the asymmetric coalescence of two sessile droplets with different sizes, the smaller droplet will travel longer distance than the larger one before coalescence because of the stronger capillary driving force for the smaller droplet. Note that both small and large droplets are initially located at the same distance form the computational domain center in the x direction. If $R_{r2} > R_{r1}$ (see Fig. 2), the coalescence will take place at $x > 0$; otherwise, it will take place at $x < 0$. In any case, once the two droplets meet each other, a capillary bridge will form, and two droplets will merge to one bigger droplet. Figure 7 shows some snapshots of the coalescence process between two sessile droplets with $R_{r1} = 1$ and $R_{r2} = 0.5$. The second snapshot [Fig. 7(b)] shows the shape of the two droplets when a capillary bridge forms a neck between the two droplets. The forth snapshot [Fig. 7(d)] is at a late stage of the coalescence when the neck disappears due to the expansion of the capillary bridge. The fifth snapshot [Fig. 7(e)] shows an asymmetric ellipsoid shape of the merged droplet before the end of the coalescence process. Finally, Fig. 7(f) shows the final shape of the merged microdroplet at the end of the coalescence.

The shape change at different stages of the coalescence shown in Fig. 7 can be explained by the flow inside the merged droplet. As an example, Fig. 8 shows velocity vectors in the Fig. 7(d). Note that in Fig. 8 the length of the velocity vector is proportional to its absolute value. Different from symmetric coalescence in the baseline case (see Fig. 5), Fig. 8 shows that there is faster flow inside the smaller side of the merged droplet than that in the bigger side. This is because there is higher capillary driving force from the larger curvature of the free surface at the smaller side of the merged droplet. As a result, the smaller droplet is absorbed into the bigger droplet.

For further quantitative analysis, the growth of the capillary bridge (W_m and H_m) with time (τ) is plotted in Fig. 9 for three different cases ($R_{r2} = 0.5$, 1.0, and 1.5). It shows that an increase in R_{r2} leads to larger W_m and H_m. This is due to the increasing in the volume of fluid flow towards the capillary bridge by increasing R_{r2}. Same as the discussion

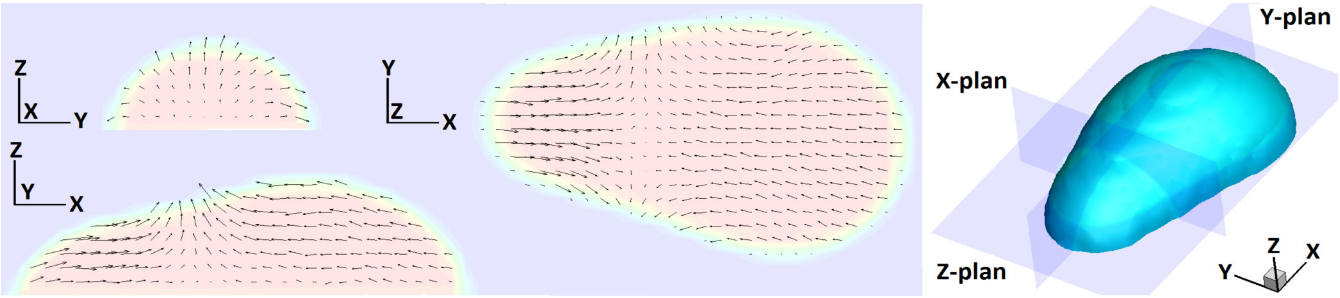

FIG. 8. Flow velocity vectors on the x, y, and z planes for Fig. 7(d).

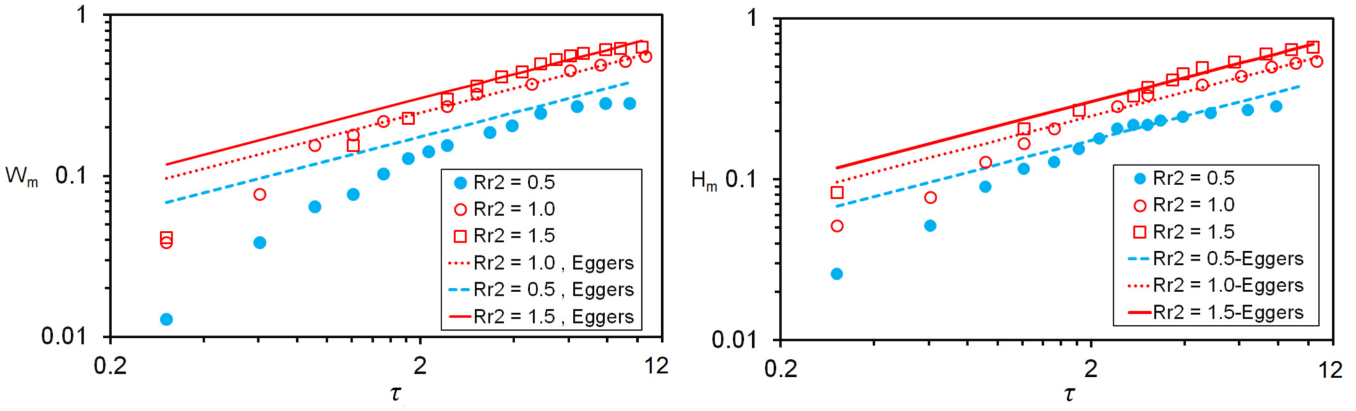

FIG. 9. Variation of W_m and H_m with time for different values of R_{r2} in the early stage of the coalescence process. Predicted lines for W_m and H_m by Eggers's model [Eq. (13)] also have been plotted. Note that both the x and the y axes are in $\log_{10}$ scale.

on the baseline case in Sec. III A, we consider that the growth rates of W_m and H_m follow a power law, i.e., $H_m = \beta_1 \tau^\beta$ and $W_m = \alpha_1 \tau^\alpha$. The values of β and α are extracted out from numerical results in the early stage of coalescence processes and listed in Table II. It shows that the values of β and α are around 0.5, which is close to the values reported in the literature [17,19].

Moreover the results have been compared with the theoretical model given by Eggers *et al.* for free coalescence [10]. According to the Eggers's model, the neck radius grows proportionally with the square root of the coalescence time. With the model parameters adopted in the current study, Eggers's model is given as

$$H_m = W_m = C\frac{1}{2\sigma}\left(\frac{R_2}{\rho}\right)^{\frac{1}{4}}\frac{\mu^{5/8}}{R_0^{1/2}}\tau^{1/2}, \qquad (13)$$

where C is an empirical coefficient close to 1 as reported in the literature [11]. For comparison, we plotted the theoretical results based on Eq. (13) with $C = 1$ together in Fig. 9. It shows that there is good agreement between current numerical results and the theoretical results. However, the model predicts larger H_m and R_m at the beginning of the coalescence process. This is because the effects from the solid substrate are not considered in the predictions.

C. Coalescence between a moving and a stationary sessile droplet

Another type of the asymmetric coalescence process happens when a stationary sessile droplet and a moving sessile droplet are coalesced together. To study this process, we consider two differences from the baseline model. First, a uniform wettability property ($\theta = \theta_f$) is adopted on the solid substrate for $x \leqslant 0.0$, and second, it is assumed that L_2 is 10.0.

TABLE II. Calculated value of β and α in $H_m = \beta_1 \tau^\beta$ and $W_m = \alpha_1 \tau^\alpha$, respectively.

R_{r1}	R_{r2}	β	α
1.0	0.5	0.59	0.50
1.0	1.0	0.54	0.55
1.0	1.5	0.57	0.55

Once computations triggered, both droplets start to adopt themselves with the wettability properties on the solid surface. Then the droplet located on the solid substrate subject to the wetting gradient ($x > 0.0$) begins to move towards the center ($x = 0.0$). Then the coalescence process is initiated close to the center with $x < 0.0$. After the capillary bridge is formed, the liquid flow from inside both droplets starts to move into the liquid bridge. The flow direction inside the liquid bridge is to expand the bridge in y and z directions.

Figure 10 shows some snapshots of the interfacial development and evolution of the coalescence process between a pair of sessile microdroplets. The left microdroplet is moving and the right microdroplet is stationary.

Moreover, Fig. 11 shows some snapshots of the trimmed 3D streamlines released from arbitrarily selected x planes towards the liquid bridge when coalescence proceeds. The time sequence is from left to right. Figure 12 shows flow velocity vectors on the x, y, and z planes once the merged droplet forms almost an elongated ellipsoid shape during the coalescence process. Velocity vectors on the y plane clearly shows that inside the stationary droplet the flow rate towards the liquid bridge is higher comparing to that of the moving droplet.

For further analysis, variations of W_m and H_m with time have been shown in Fig. 13. These results are for the solid surfaces with different phobicity but same wetting gradient properties. Moreover, results are for the early stage of the coalescence process. It shows that increasing the phobicity of the surface makes both W_m and H_m grow faster. This is because that there is stronger capillary driving force and less viscous dissipation on the more phobic surface due to the smaller radius of curvature as well as the smaller liquid-solid interfacial area. Note that although it is not presented here, the final value of W_m on the philic surface at the end of the late-stage coalescence will be larger than that of for the W_m value on the phobic surface.

D. Comparison between the symmetric and the asymmetric coalescence processes

It is of interest to perform a quantitative comparison between results of W_m and H_m from asymmetric coalescence (Sec. III C) with those from symmetric coalescence

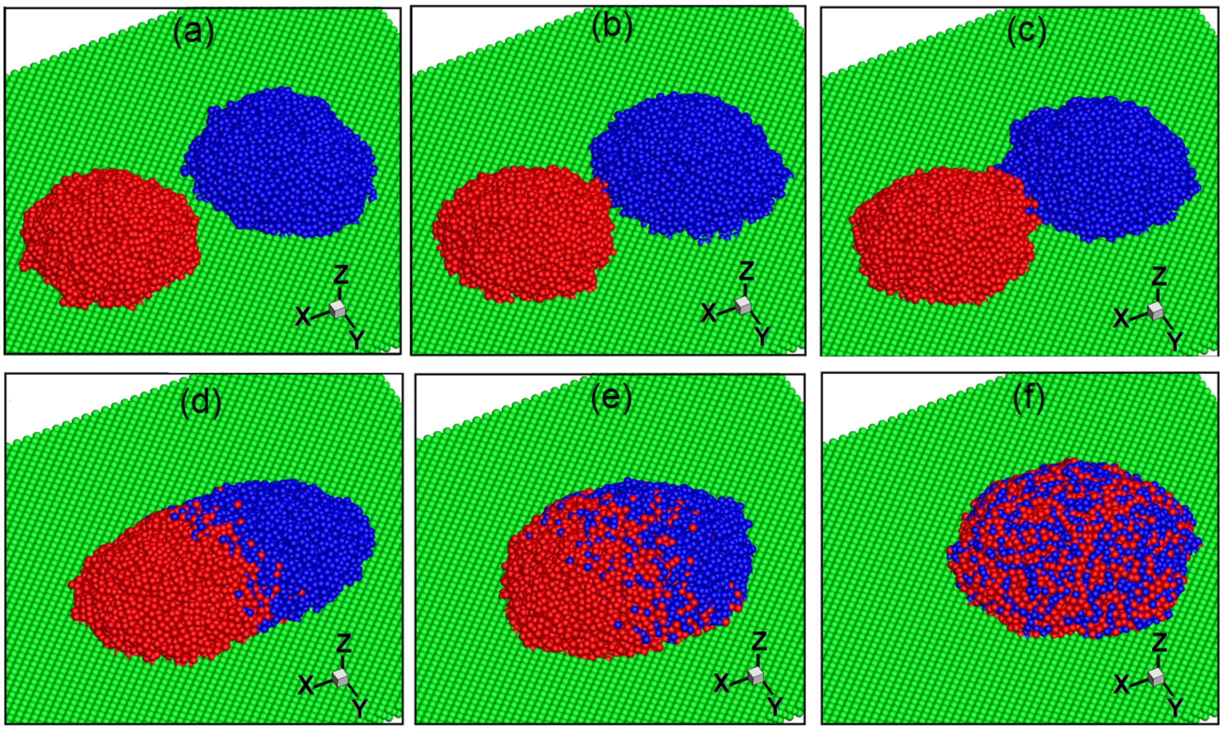

FIG. 10. Snapshots of the interfacial development and evolution of the coalescence process between a pair of sessile microdroplets. The left microdroplet is moving and the right microdroplet is stationary. Note that time sequence is from (a) to (f).

(Sec. III A). Such comparison has been shown in Fig. 14. In this figure, results of W_m and H_m at two different wetting gradients have been plotted. In both cases θ_f is 82°, but for one case θ_0 is 90°, while for the other one θ_0 is 100°. As Fig. 14 indicates, if the adopted wetting gradient is small, e.g., $\theta_0 = 90^\circ$ and $\theta_f = 82^\circ$, then the difference between results of symmetric and asymmetric coalescence will be negligible. However, if the applied wetting gradient is large, e.g., $\theta_0 = 100^\circ$ and $\theta_f = 82^\circ$, then the difference will be pronounced. Moreover, for the asymmetric coalescence both W_m and H_m will be larger compared to the results of the symmetric coalescence. The possible explanation for this is that before initiation of the asymmetric coalescence the stationary droplet has spread more on the solid surface. Once the coalescence starts, the formed capillary bridge will have larger curvature compared to the bridge's curvature formed in symmetric coalescence. So this will produce higher flow rate and, consequently, faster growth rate.

Because viscous forces are the main reason for dissipation of the system free energy and oscillations [9], similar to the symmetric coalescence process, we do not find any oscillation for the merged droplet during the coalescence process.

IV. CONCLUSION

In this numerical research, we studied 3D flow structure inside the coalescing sessile microdroplets. This study was focused on the coalescence process between a pair of micron-sized sessile droplets on the impermeable solid surface. To drive the droplets on the solid substrate, a linear wetting gradient was applied on the solid surface. Considering the Brownian motion associated with the micron-sized sessile droplets, a *many-body dissipative particle dynamics* (MDPD) method was adopted in this numerical study. Thorough analysis was conducted to understand the flow structure inside the

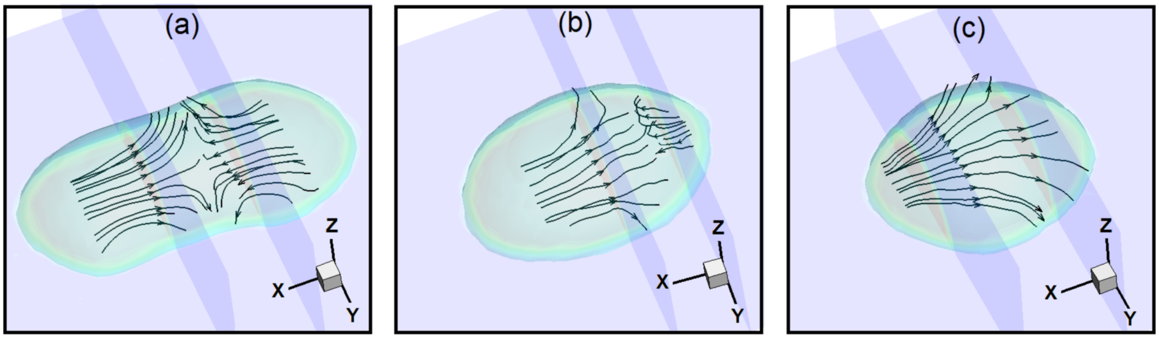

FIG. 11. Trimmed 3D flow streamlines inside the merged droplet at different arbitrary times during the asymmetric coalescence process. Streamlines are released from arbitrarily selected x planes.

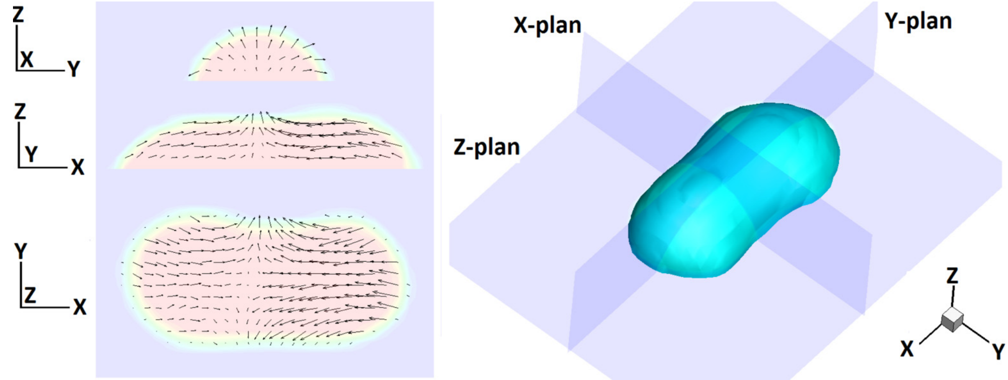

FIG. 12. Flow velocity vectors on x, y, and z planes when the merged droplet reaches to an elongated ellipsoid shape in an asymmetric coalescence process.

merged droplet in both symmetric and asymmetric coalescence processes.

Moreover, a comprehensive parametric study was carried out to investigate the effects of the wettability gradient and philicity of the solid surface on the coalescence process. In particular, these effects were studied on the flow structures and on the externally measurable parameters, e.g., formed liquid bridge radius. Special attention was given to the growth rate of the liquid bridge's radius parallel to the solid substrate (W_m) and perpendicular to the solid substrate (H_m). In particular, the results in the early stage of the coalescence process were compared with those in the literature.

Flow structure analysis shows that in both symmetric and asymmetric coalescence processes the liquid flow direction inside the capillary bridge is to expand the bridge radius in y and z directions. However, the capillary bridge does not expand with same speed and rate in all directions. Surface philicity, wetting gradient, droplet size, and asymmetric and symmetric coalescence affect the expansion rate. Furthermore, the direction of the liquid flow inside the liquid bridge remains almost unchanged until the end of the late stage of the coalescence process.

Further analysis shows that the formed contact zone between to merging droplets grows against the droplet motion in the x direction. In the symmetric coalescence, the contact zone grows at the same rate against the motion of both merging droplets. However, in asymmetric coalescence when one of the droplets is small, the contact zone grows towards the small droplet's far end.

Besides, the results indicate that the growth rates of W_m and H_m fall in very good agreement with the reported trends in the literature. On the more philic surface subject to a defined wetting gradient, W_m grows faster than H_m and reaches the higher values by end of the early stage of the coalescence process. However, increasing the surface phobicity moderates this behavior. Further increase in surface phobicity leads to the faster growth of the liquid bridge in the direction perpendicular to the solid substrate. Moreover, an increase in the wetting gradient increases the difference between reported W_m and H_m values for symmetric and asymmetric coalescence processes.

Finally, due to the significant effects of the viscous forces, the oscillation of the merged droplet during the coalescence process is not observed.

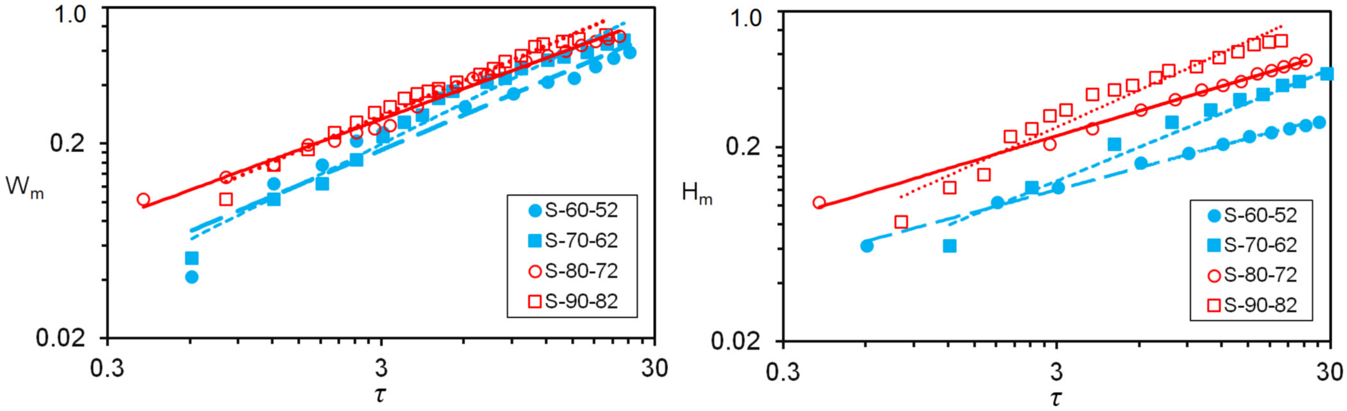

FIG. 13. Variation of W_m and H_m with time when one a sessile droplet moves towards a stationary droplet. A constant wetting gradient has been applied on the solid surfaces. However, the surface has different philicity properties. Note that the results are for the early stage of the coalescence process. Note that both the x and the y axes are in $\log_{10}$ scale.

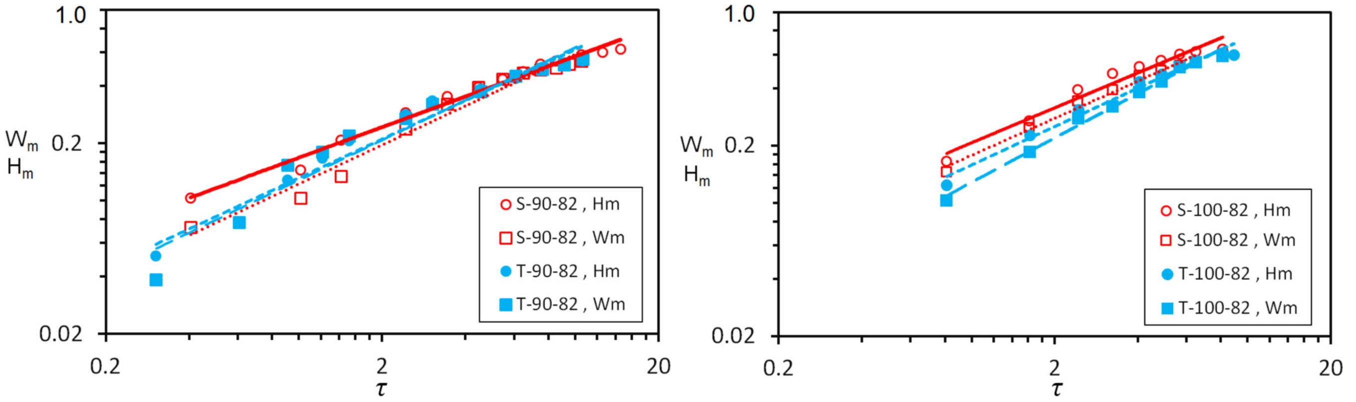

FIG. 14. Comparison of W_m and H_m trends in time between symmetric and asymmetric coalescence. T-90-82-Wm, T-90-82-Hm, T-100-82-Wm, and T-100-82-Hm are for the case that both droplets move on the solid surface (symmetric coalescence). S-90-82-Wm, S-90-82-Hm, S-100-82-Wm, and S-100-82-Hm are for the cases that only one of the droplets moves while the other one is stationary (asymmetric coalescence). Note that the results are for the early stage of the coalescence process, and both the x and the y axes are in $\log_{10}$ scale.

[1] J. Qian and C. K. Law, J. Fluid Mech. **331**, 59 (1997).
[2] A. Menchaca-Rocha, A. Martínez-Dávalos, R. Nunez, S. Popinet, and S. Zaleski, Phys. Rev. E **63**, 046309 (2001).
[3] C. Andrieu, D. A. Beysens, V. S. Nikolayev, and Y. Pomeau, J. Fluid Mech. **453**, 427 (2002).
[4] A. L. Yarin, G. G. Chase, W. Liu, S. V. Doiphode, and D. H. Reneker, AIChE J. **52**, 217 (2006).
[5] J. Kim and E. K. Longmire, Exp. Fluids **47**, 263 (2009).
[6] S. Quan, J. Lou, and D. P. Schmidt, J. Comput. Phys. **228**, 2660 (2009).
[7] S. Quan, J. Comput. Phys. **230**, 5430 (2011).
[8] N. Ashgriz, *Handbook of Atomization and Sprays* (Springer, Heidelberg, New York, 2011).
[9] Y.-H. Lai, M.-H. Hsu, and J.-T. Yang, Lab Chip **10**, 3149 (2010).
[10] J. Eggers, J. R. Lister, and H. A. Stone, J. Fluid Mech. **401**, 293 (1999).
[11] D. G. A. L. Aarts, H. N. W. Lekkerkerker, H. Guo, G. H. Wegdam, and D. Bonn, Phys. Rev. Lett. **95**, 164503 (2005).
[12] J. D. Paulsen, Phys. Rev. E **88**, 063010 (2013).
[13] J. D. Paulsen, R. Carmigniani, A. Kannan, J. C. Burton, and S. R. Nagel, Nat. Commun. **5**, 3182 (2014).
[14] N. Kapur and P. H. Gaskell, Phys. Rev. E **75**, 056315 (2007).
[15] R. Narhe, D. Beysens, and Y. Pomeau, Europhys. Lett. **81**, 46002 (2008).
[16] J. F. Hernandez-Sanchez, L. A. Lubbers, A. Eddi, and J. H. Snoeijer, Phys. Rev. Lett. **109**, 184502 (2012).
[17] Y. Sui, M. Maglio, P. D. M. Spelt, D. Legendre, and H. Ding, Phys. Fluids **25**, 101701 (2013).
[18] M. Ahmadlouydarab and J. J. Feng, J. Fluid Mech. **746**, 214 (2014).
[19] M. W. Lee, D. K. Kang, S. S. Yoon,, and A. L. Yarin, Langmuir **28**, 3791 (2012).
[20] A. M. Cazabat, F. Heslot, S. M. Troian, and P. Carles, Nature (London) **346**, 824 (1990).
[21] M. K. Chaudhury and G. M. Whitesides, Science **256**, 1539 (1992).
[22] B. Gallardo, F. Eagerton, L. Jong, V. Craig, R. Shah, and N. Abbott, Science **283**, 57 (1999).
[23] S. Daniel and M. K. Chaudhury, Langmuir **18**, 3404 (2002).
[24] S.-H. Choi and B. Z. Newby, Langmuir **19**, 7427 (2003).
[25] M. S. Kim, K. S. Seo, G. Khang, and H. B. Lee, Bioconjugate Chem. **16**, 245 (2005).
[26] X. Jiang, Q. Xu, S. K. W. Dertinger, A. D. Strook, T. Fu, and G. M. Whitesides, Anal. Chem. **77**, 2338 (2005).
[27] N. Moumen, R. S. Subramanian, and J. B. McLaughlin, Langmuir **22**, 2682 (2006).
[28] K. A. Wier and T. J. McCarthy, Langmuir **22**, 2433 (2006).
[29] X. Yu, Z. Wang, Y. Jiang, and X. Zhang, Langmuir **22**, 4483 (2006).
[30] B. P. Harris and A. T. Metters, Macromolecules **39**, 2764 (2006).
[31] A. Shastry, M. J. Case, and K. F. Bohringer, Langmuir **22**, 6161 (2006).
[32] Y. Ito, M. Heydari, A. hashimoto, T. Konno, A. Hirasawa, S. Hori, K. Kurita, and A. Nakajima, Langmuir **23**,1845 (2007).
[33] J. R. Castrejon-Pita, E. S. Betton, K. J. Kubiak, M. C. T. Wilson, and I. M. Hutchings, Biomicrofluidics **5**, 014112 (2011).
[34] R. Narhe, D. Beysens, and V. S. Nikolayev, Langmuir **20**, 1213 (2004).
[35] S. J. Gokhale, S. Das Gupta, J. L. Plawsky, and P. C. Wayner, Phys. Rev. E **70**, 051610 (2004).
[36] J. Madejski, Int. J. Heat Mass Transfer **19**, 1009 (1976).
[37] P. Paik, V. K. Pamula, M. G. Pollack, and R. B. Fair, Lab Chip **3**, 28 (2003).
[38] C. Wang, N. T. Nguyen, and T. N. Wong, Sens. Actuators A: Phys. **133**, 317 (2007).
[39] W. D. Ristenpart, P. M. McCalla, R. V. Roy, and H. A. Stone, Phys. Rev. Lett. **97**, 064501 (2006).
[40] Y.-H. Lai, J.-T. Yang, and D.-B. Shieh, Lab Chip **10**, 499 (2010).
[41] P. B. Warren, Phys. Rev. E **68**, 066702 (2003).
[42] E. Moeendarbary, T. Y. Ng, and M. Zangeneh, Int. J. Appl. Mech. **01**, 737 (2009).
[43] Z. Li, G. H. Hu, Z.-L. Wang, Y.-B. Ma, and Z.-W. Zhou, Phys. Fluids **25**, 072103 (2013).

[44] C. Lan, S. Pal, Z. Li, and Y. b. Ma, Langmuir **31**, 9636 (2015).

[45] E. E. Keaveny, I. V. Pivkin, M. Maxey, and G. E. Karniadakis, J. Chem. Phys. **123**, 104107 (2005).

[46] B. Henrich, C. Cupelli, M. Moseler, and M. Santer, Europhys. Lett. **80**, 60004 (2007).

[47] C. Cupelli, B. Henrich, T. Glatzel, R. Zengerle, M. Moseler, and M. Santer, New J. Phys. **10**, 043009 (2008).

[48] P. A. Thompson and M. O. Robbins, Phys. Rev. Lett. **63**, 766 (1989).

[49] R. G. Cox, J. Fluid Mech. **168**, 169 (1986).

[50] R. D. Groot and P. B. Warren, J. Chem. Phys. **107**, 4423 (1997).

[51] N. G. Hadjiconstantinou, Phys. Fluids **18**, 111301 (2006).

[52] L. Duchemin, J. Eggers, and C. Josserand, J. Fluid Mech. **487**, 167 (2003).